

# Understanding H<sub>2</sub> Evolution Electrochemistry to Minimize Solvated Water Impact on Zinc-Anode Performance

Fuhua Yang, Jodie A. Yuwono, Junnan Hao, Jun Long, Libei Yuan, Yanyan Wang, Sailin Liu, Yameng Fan, Shiyong Zhao, Kenneth Davey, and Zaiping Guo\*

H<sub>2</sub> evolution is the reason for poor reversibility and limited cycle stability with Zn-metal anodes, and impedes practical application in aqueous zinc-ion batteries (AZIBs). Here, using a combined gas chromatography experiment and computation, it is demonstrated that H<sub>2</sub> evolution primarily originates from solvated water, rather than free water without interaction with Zn<sup>2+</sup>. Using linear sweep voltammetry (LSV) in salt electrolytes, H<sub>2</sub> evolution is evidenced to occur at a more negative potential than zinc reduction because of the high overpotential against H<sub>2</sub> evolution on Zn metal. The hypothesis is tested and, using a glycine additive to reduce solvated water, it is confirmed that H<sub>2</sub> evolution and “parasitic” side reactions are suppressed on the Zn anode. This electrolyte additive is evidenced to suppress H<sub>2</sub> evolution, reduce corrosion, and give a uniform Zn deposition in Zn|Zn and Zn|Cu cells. It is demonstrated that Zn|PANI (highly conductive polyaniline) full cells exhibit boosted electrochemical performance in 1 M ZnSO<sub>4</sub>–3 M glycine electrolyte. It is concluded that this new understanding of electrochemistry of H<sub>2</sub> evolution can be used for design of relatively low-cost and safe AZIBs for practical large-scale energy storage.

## 1. Introduction

In recent decades there has emerged significant research interest in aqueous zinc-ion batteries (AZIBs) as a practically promising alternative to lithium-ion batteries.<sup>[1,2]</sup> The reasons include, low relative cost, good environmental “friendliness” and nonflammability.<sup>[3–7]</sup> Zinc metal is widely used as an anode in AZIBs because it exhibits a high theoretical capacity of 820 mAh g<sup>-1</sup> and a low electrochemical potential of –0.762 V versus SHE which results in an attractive energy density in practical application.<sup>[8,9]</sup>

Obstacles to the practical use of zinc-metal anodes originate from a relatively negative reduction potential for Zn of –0.762 V versus standard hydrogen electrode (SHE), leading to H<sub>2</sub> evolution and changing the local pH to strong alkaline.<sup>[10–12]</sup> The alkaline environment cor-

rodes the Zn anode via side reactions, leading to poor electrochemical performance including, low Coulombic efficiency (CE) and rapid capacity decay. Additionally, an obstacle is the formation of Zn dendrite and the resulting cell short-circuit.<sup>[13,14]</sup> Therefore, suppression of H<sub>2</sub> evolution and inhibition of Zn dendrite growth on Zn-metal anodes are necessary for high-performance and safe AZIBs.

Zn anode structural engineering, artificial protection layer construction, and electrolyte formulation have been proposed to obviate these obstacles.<sup>[15–18]</sup> However, relatively complex fabrication, high production cost, and low volumetric energy density hinder structural engineering and artificial protection layers at scale.<sup>[19,20]</sup>

The present understanding of H<sub>2</sub> evolution electrochemistry and low-cost electrolyte formulation is poor. In a typical zinc-ion electrolyte, Zn<sup>2+</sup> solvated with six water molecules forms hydrated zinc ions [Zn(H<sub>2</sub>O)<sub>6</sub>]<sup>2+</sup>.<sup>[21]</sup> It is not known whether H<sub>2</sub> evolution originates primarily from solvated water molecules or free water molecules. Preliminary theoretical computation implies that interaction between H<sub>2</sub>O and Zn<sup>2+</sup> weakens the O–H bond of H<sub>2</sub>O, leading to deprotonation of the solvated water and research to reduce the solvated water population.<sup>[22,23]</sup> On the other hand, research with a focus on minimizing free water activity has evidenced the importance of the H<sub>2</sub> evolution of free water in zinc-anode performance.<sup>[24,25]</sup>

Additionally, the H<sub>2</sub> evolution potential in zinc-ion electrolyte is not reliably known. Thermodynamically, zinc metal is


F. Yang, J. A. Yuwono, J. Hao, L. Yuan, Y. Wang, S. Liu, S. Zhao, K. Davey, Z. Guo

School of Chemical Engineering and Advanced Materials  
The University of Adelaide  
Adelaide SA 5005, Australia  
E-mail: zaiping.guo@adelaide.edu.au

F. Yang, L. Yuan, Y. Fan  
Institute for Superconducting and Electronic Materials  
School of Mechanical, Materials, Mechatronics and Biomedical Engineering  
University of Wollongong  
North Wollongong NSW 2522, Australia

J. A. Yuwono  
College of Engineering and Computer Science  
Australian National University  
Canberra, ACT 2601, Australia

J. Long  
Shenzhen Geim Graphene Center  
Tsinghua-Berkeley Shenzhen Institute & Tsinghua Shenzhen International Graduate School  
Tsinghua University  
Shenzhen 518055, P. R. China

 The ORCID identification number(s) for the author(s) of this article can be found under <https://doi.org/10.1002/adma.202206754>.

© 2022 The Authors. Advanced Materials published by Wiley-VCH GmbH. This is an open access article under the terms of the Creative Commons Attribution-NonCommercial License, which permits use, distribution and reproduction in any medium, provided the original work is properly cited and is not used for commercial purposes.

DOI: 10.1002/adma.202206754

unstable during charge/discharge because the theoretical Zn<sup>2+</sup>/Zn redox potential of −0.76 V versus SHE is less than that for H<sub>2</sub> evolution of −0.41 V versus SHE, pH 7.<sup>[26,27]</sup> The high overpotential against H<sub>2</sub> evolution on zinc metal could practically move H<sub>2</sub> evolution to a more-negative potential.<sup>[16,28]</sup> Some reports attribute the onset reduction potential of the electrolyte to the H<sub>2</sub> evolution. However, this reasoning is not convincing because zinc reduction occurs also at a similar potential.<sup>[29,30]</sup>

It is important therefore to understand the impact of Zn<sup>2+</sup>–H<sub>2</sub>O chemistry on H<sub>2</sub> evolution and the evolution of potential rational battery design.

It is important also to understand practical electrolyte formulation, cost and environmental impact of the electrolyte.<sup>[31]</sup> Recently, solid additives have been used to control Zn<sup>2+</sup>-solvation structure because of their relatively low-cost and environmental friendliness. However, a limited zinc-ion coordination of these additives results in limited replacement of solvated water in the inner solvation shell.<sup>[32,33]</sup> Concentrated electrolytes and organic additive can prevent the formation of hydrated zinc ions [Zn(H<sub>2</sub>O)<sub>6</sub>]<sup>2+</sup> or, significantly weaken free water activity.<sup>[24,34]</sup> However, in many of these cases, boosted electrochemical performance is achieved only at a high cost or loss of environmental friendliness of AZIBs because these additives are costly and /or toxic.<sup>[35]</sup>

Here, we report for the first time using judiciously combined gas chromatography (GC) experiment and computation that solvated water is relatively unstable and subject to H<sub>2</sub> evolution compared with free water in the electrolyte and that H<sub>2</sub> evolution primarily originates from solvated water, rather than free water without interaction with Zn<sup>2+</sup>.

We show that H<sub>2</sub> evolution becomes pronounced as the proportion of solvated water molecules increases in the electrolyte. We evidence, using linear sweep voltammetry (LSV) in salt electrolytes that H<sub>2</sub> evolution occurs at a more negative potential than zinc reduction, and widening the voltage gap window between H<sub>2</sub> evolution and zinc reduction boosts zinc-anode performance. We test our hypothesis and confirm using glycine additive to reduce solvated water in the electrolyte, that H<sub>2</sub> evolution and “parasitic” side reactions are suppressed, and protect the Zn anode. Importantly, glycine is a low-cost and environmentally “friendly” solid, additive.

We show via Raman spectroscopy, Fourier-transform infrared (FT-IR) spectroscopy and density functional theory (DFT) computation, that glycine coordinates with zinc ions through amino and carboxyl function group to replace water molecules in the inner solvation shell, and reduces the solvated H<sub>2</sub>O number from 6 in [Zn(H<sub>2</sub>O)<sub>6</sub>]<sup>2+</sup> to 3 with 3 M glycine in 1 M ZnSO<sub>4</sub> electrolyte. We evidence that this new electrolyte suppresses H<sub>2</sub> evolution, reduces corrosion and gives a uniform Zn deposition in Zn|Zn, and Zn|Cu cells when compared with bare ZnSO<sub>4</sub> electrolyte.

We confirm the solvation structure electrolyte exhibits stable cycling performance in Zn|Zn symmetric half cells and exhibits a high average CE of 99.3% in Zn|Cu asymmetric cells because of suppression of H<sub>2</sub> evolution from a reduction in solvated water molecules in the electrolyte. We demonstrate Zn|PANI (highly conductive polyaniline) full cells exhibit boosted electrochemical performance in 1 M ZnSO<sub>4</sub>–3 M glycine electrolyte and, a high reversible capacity of 100 mAh g<sup>−1</sup> in a practical Zn|PANI pouch cell.

We conclude that this new understanding of electrochemistry of H<sub>2</sub> evolution is applicable to the design of relatively low-cost and safe AZIBs for large-scale, practical energy storage. Findings will be of immediate benefit in electrolyte design for high-performance rechargeable batteries and therefore of wide interest to researchers and manufacturers.

## 2. Results and Discussion

### 2.1. H<sub>2</sub> evolution and Correlation with Solvated Water

FT-IR and Raman spectroscopy were used to determine the correlation between H<sub>2</sub> evolution and solvated water in the electrolyte, and the evolution of solvated water ratio in electrolytes. The FT-IR spectrum exhibited a positive shift and peak intensity weakening of the O–H vibrations band as concentration increased, **Figure 1a**, evidencing reduced free water molecules in the concentrated electrolyte.<sup>[34]</sup> (Concentrations denoted “m” and “M” are, respectively, the molarity of the salt or additive, with respect to DI water and total electrolyte volume). **Figure 1b** presents the Raman spectra in which a broad band extending from 3000 to 3800 cm<sup>−1</sup> originating from the O–H stretching mode for H<sub>2</sub>O can be seen for all concentration spectra. Analyses of the Raman spectra via Gaussian fitting showed that the O–H stretching vibration can be devolved into three components, confirming three types of O–H stretching vibration. The low-wavenumber component and main component are attributed to, respectively, 4-coordinated hydrogen-bonded water (4-HB·H<sub>2</sub>O) and 2-coordinated hydrogen-bonded water (2-HB·H<sub>2</sub>O), whilst the high wavenumber component is attributed to Zn<sup>2+</sup>-solvated water (Zn·H<sub>2</sub>O), **Figure 1c** (and **Figure S1**, Supporting Information).<sup>[36–38]</sup> As salt concentration increases, the hydrogen-bond interaction decreases, whilst the Zn<sup>2+</sup>–H<sub>2</sub>O interaction strengthens, **Figure 1b**. The proportion of solvated water computed from the area of fitted peaks (**Figure S2**, Supporting Information), confirmed that the solvated water population increases (gradually) with salt concentration. Solvated water ratio increased from 8.7% in 1 m ZnCl<sub>2</sub> to 25% in 10 m ZnCl<sub>2</sub>, and remained constant at ≈26% in greater concentrations of 15, 20, and 30 m, **Figure 1d**.

H<sub>2</sub> evolution in a range of concentrations of electrolyte was determined by immersing identical zinc foils in ZnCl<sub>2</sub> electrolytes (**Figure S2**, Supporting Information) in sealed vials, which were subjected to GC measurement to quantify H<sub>2</sub> released. As is shown in the GC spectra **Figure 1e**, there are two peaks centered at 4.7 and 4.98 min that are attributed to, respectively, H<sub>2</sub> released from the zinc metal, and O<sub>2</sub> originating from the air. The intensity of O<sub>2</sub> remains constant across salt concentrations, confirming that no O<sub>2</sub> is released in the electrolyte other than that O<sub>2</sub> in the air. The H<sub>2</sub> peak exhibits an upward trend with intensity from a concentration of 1 to 10 m and significantly decreases with greater concentrations of 15, 20, and 30 m ZnCl<sub>2</sub> electrolyte, **Figure 1f**. H<sub>2</sub> content was computed from GC spectra as shown in **Figure 1g**. H<sub>2</sub> in 1 m ZnCl<sub>2</sub> is 4.54 μmol L<sup>−1</sup>. It steadily increased with concentration, respectively, 7.66, 12.29, and 15.15 μmol L<sup>−1</sup> in 3, 5, and 7 m electrolyte, and was a maximum of 18.46 μmol L<sup>−1</sup> in 10 m ZnCl<sub>2</sub> electrolyte. However, with increased concentration to 15, 20, and 30 m, it

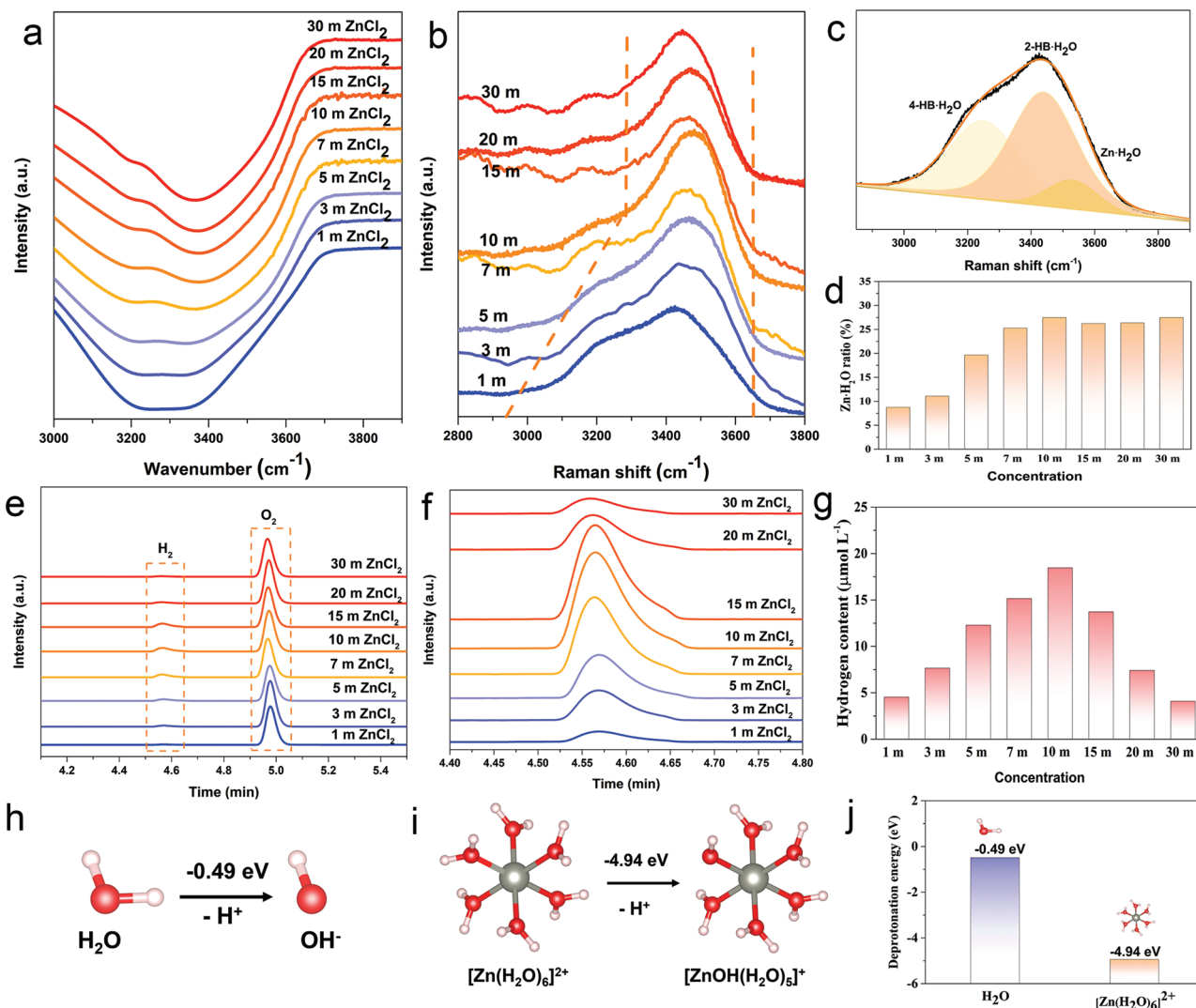


**Figure 1.** Hydrogen evolution in salt-concentrated electrolyte and correlation with solvated water. a) FT-IR spectra for ZnCl<sub>2</sub> electrolytes; b) Raman O–H stretching vibration for electrolytes. c) Fitted O–H stretching vibration associated with 4-coordinated hydrogen-bonded water (4-HB-H<sub>2</sub>O), 2-coordinated hydrogen-bonded water (2-HB-H<sub>2</sub>O) and Zn<sup>2+</sup>-ion-hydrated water (Zn-H<sub>2</sub>O). d) Zn-H<sub>2</sub>O water ratio. e) Gas chromatography (GC) profile, f) enlarged H<sub>2</sub> signals in ZnCl<sub>2</sub> electrolytes, and g) corresponding H<sub>2</sub> in tested electrolyte. h–j) Deprotonation energy via DFT computation for free H<sub>2</sub>O (h), and solvated [Zn(H<sub>2</sub>O)<sub>6</sub>]<sup>2+</sup> (i).

exhibited a reduced H<sub>2</sub> evolution. The GC results reveal that H<sub>2</sub> evolution on zinc metal is concentration-dependent.

As seen in the Raman and GC findings, in low concentrations of 1 to 10 m electrolyte, H<sub>2</sub> evolution increased as the solvated water ratio increased. This is attributed to the Zn<sup>2+</sup>-H<sub>2</sub>O interaction. Zn<sup>2+</sup> ions solvate with water molecules to form highly oriented and ordered hydrated zinc ions [Zn(H<sub>2</sub>O)<sub>6</sub>]<sup>2+</sup> in the zinc electrolyte because of the electropositivity of Zn<sup>2+</sup> and polar nature of water molecule.<sup>[21]</sup> The Zn<sup>2+</sup>-H<sub>2</sub>O interaction in [Zn(H<sub>2</sub>O)<sub>6</sub>]<sup>2+</sup> significantly reduces the O–H bond strength of the solvated water molecules, and as a result, accelerates H<sub>2</sub> evolution in the aqueous electrolyte.

To confirm this the deprotonation energy for free, and solvated, water was computed using DFT at, respectively, –0.49 and –4.94 eV, underscoring deprotonation of solvated H<sub>2</sub>O is more

energetically favorable than for the free states, Figure 1h–j. The suppression of H<sub>2</sub> evolution with greater concentration can be explained by the scarcity of water, given that H<sub>2</sub>O content is, respectively, just 34.3, 28.21, and 22.17 mmol in 1 mL 15, 20, and 30 m ZnCl<sub>2</sub> electrolytes (Figure S3, Supporting Information).

## 2.2. Identification of Zn Deposition and H<sub>2</sub> Evolution Onset Voltage

To determine H<sub>2</sub> evolution and Zn reduction potential on the zinc-metal anode, linear sweep voltammetry (LSV) measurement was performed on electrolytes with differing salt concentration. In zinc-ion electrolyte, Zn reduction and H<sub>2</sub> evolution occur at a similar reduction voltage. Therefore, to exclude any impact of

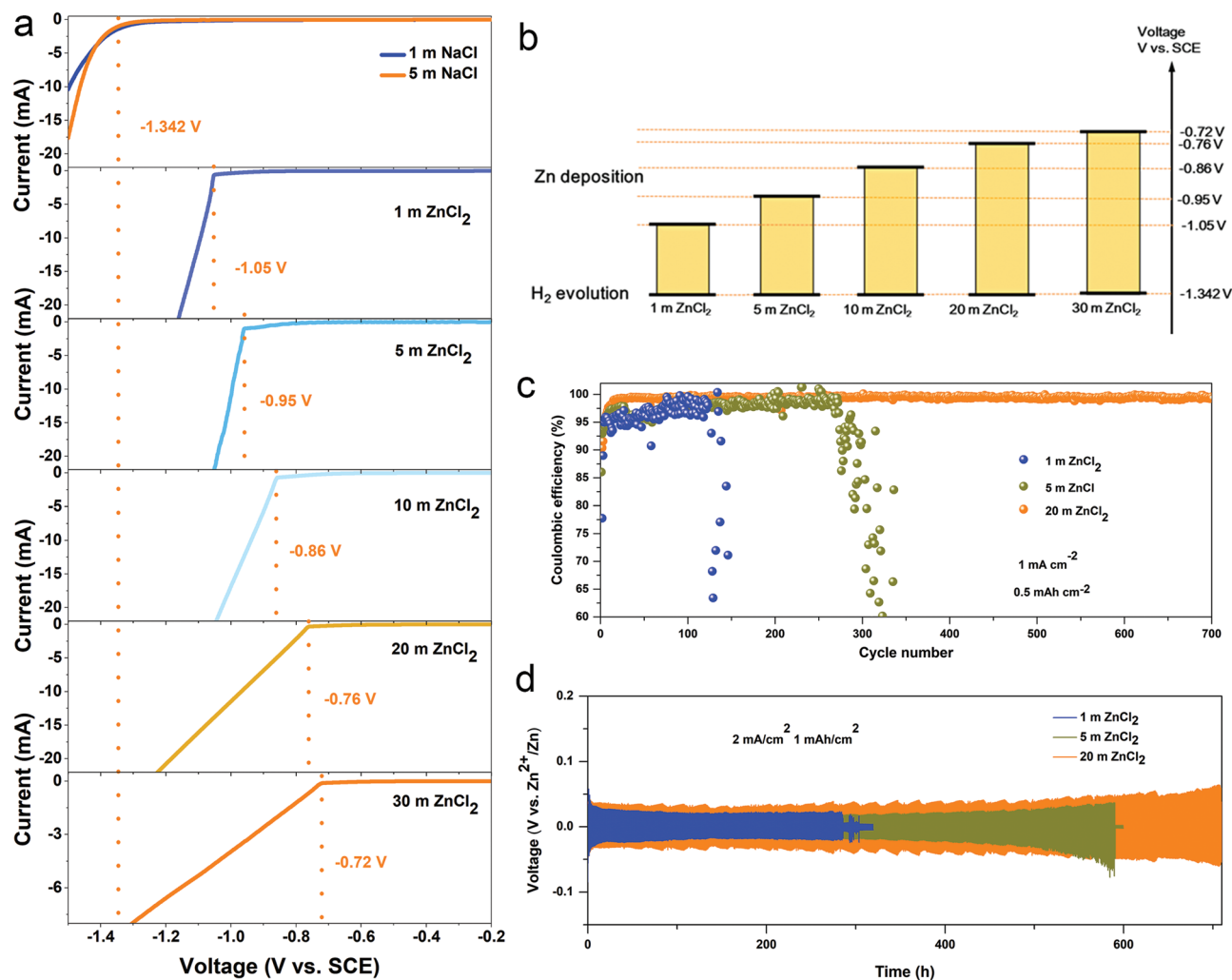


**Figure 2.** Identification of Zn deposition and H<sub>2</sub> evolution onset voltage and impact on Zn anode performance. a) Linear sweep voltammetry (LSV) findings for NaCl and ZnCl<sub>2</sub> electrolytes, and b) corresponding voltage difference between H<sub>2</sub> evolution and Zn reduction in concentrated ZnCl<sub>2</sub> electrolyte. c) Zn|Cu asymmetric and d) Zn|Zn symmetric cell performance in different electrolytes.

Zn reduction, the NaCl solution was tested via LSV. As is shown in Figure 2a, the onset reduction of NaCl solution occurs at  $-1.342$  V (versus SCE) irrespective of salt concentration.

This finding is attributed to the H<sub>2</sub> evolution potential because there is no Zn reduction taking place in the NaCl solution. In contrast, 1 m ZnCl<sub>2</sub> features an onset reduction voltage of  $-1.06$  V, which is attributed to be the onset of Zn reduction voltage. To confirm this, greater concentration ZnCl<sub>2</sub> electrolytes were subjected to LSV measurement. A positive shift was observed in the greater concentration ZnCl<sub>2</sub> electrolyte, with reduction voltages, respectively, at  $-0.95$ ,  $-0.86$ ,  $-0.76$ , and  $-0.72$  V for 5, 10, 20, and 30 m electrolytes. This positive voltage shift results from greater Zn<sup>2+</sup> activity in greater salt concentration for Zn reduction according to the Nernst equation, namely:

$$E = E^0 + RT/2F \times (\ln a_{[\text{Zn}^{2+}]}) \quad (1)$$

for the Zn reduction reaction



Therefore it is concluded from the LSV findings, that the zinc electrolyte undergoes Zn reduction before H<sub>2</sub> evolution.

Significantly, this initially seems contrary to the theoretical electrochemical potentials for H<sub>2</sub> evolution and Zn reduction because the Zn<sup>2+</sup>/Zn redox potential of  $-0.76$  V versus SHE is less than that for H<sub>2</sub> evolution of  $-0.41$  V versus SHE, pH = 7. However, the LSV findings can be explained by the high overpotential against H<sub>2</sub> on zinc metal. As is seen in the Pourbaix diagram for the Zn electrode in aqueous media, Figure S4 (Supporting Information), although the red-color dotted line representing the theoretical H<sub>2</sub> evolution voltage is above the Zn<sup>2+</sup>/Zn reduction potential, the practical H<sub>2</sub> evolution voltage (blue dotted line) is below that for zinc reduction because of the high overpotential.<sup>[39]</sup>

Figure 2b illustrates that the voltage gap between H<sub>2</sub> evolution and Zn deposition expanded with salt concentration because the H<sub>2</sub> evolution voltage remains constant at  $-1.342$  V, whilst the zinc deposition voltage increased with salt concentration. This expanded voltage gap to minimize H<sub>2</sub> evolution and suppresses parasitic side reactions, and as a result, boosts zinc

anode performance. The reversibility of Zn plating/stripping in 1, 5, and 20 m ZnCl<sub>2</sub> electrolyte was determined in Zn|Cu asymmetric cells, Figure 2c. The low-concentration electrolyte, 1 m ZnCl<sub>2</sub>, did not exhibit long-term reversibility, whereas, the cycling stability for 5 and 20 m electrolyte significantly boosted cycle life, respectively, of 300 and 700 cycles for 5 and 20 m electrolyte.

Importantly, the CE for 20 m electrolyte increased at a more rapid pace and significantly greater than dilute counterparts, evidencing that the irreversible H<sub>2</sub> evolution and corrosion reaction on the zinc metal is significantly suppressed. In contrast to the reported concentrated electrolyte in which TFSI-based salt was used to form a protective SEI layer to prevent H<sub>2</sub> evolution, the anion-derived SEI layer was not expected.<sup>[40]</sup>

The boosting of the Zn|Cu cell performance can be explained by the expanded voltage gap between H<sub>2</sub> evolution and Zn reduction, as the Zn reduction voltage shifts positively with salt concentration and reduces H<sub>2</sub> evolution that occurs at a constant voltage below Zn<sup>2+</sup>/Zn redox voltage.

To gain an understanding of the impact of the expanded voltage gap between H<sub>2</sub> evolution and zinc reduction on zinc-dendrite formation, Zn|Zn symmetric cells were assessed with different electrolytes. Symmetric Zn|Zn cells testing confirmed the long-term cycling stability of the 5 and 20 m electrolytes, whereas, the 1 m electrolyte exhibited a voltage fall at ≈250 h which is attributed to an internal short-circuit originating from zinc-dendrite growth, Figure 2d.

### 2.3. Control of Solvation Structure to Reduce Solvated Water in Electrolyte

To test our hypothesis of the detrimental impact of solvated water on the zinc-metal anode, a solid additive, glycine, which is comparatively low cost compared with commonly used salts (Figure S5, Supporting Information) was used to control the Zn<sup>2+</sup>-solvation structure.

This glycine additive possesses one carboxy and one amino group, and reportedly has a stronger coordination ability with the metal ions than with the water molecules.<sup>[41,42]</sup> Characterization techniques, including, Raman, FT-IR, and NMR were used to determine solvation structure evolution in the ZnSO<sub>4</sub>-glycine electrolyte. The Raman spectra, Figure 3a, show that the characteristic C-N stretching vibration band located at 1035 cm<sup>-1</sup> in pure glycine solution shifts to a higher wavenumber on the addition of ZnSO<sub>4</sub> salt to the electrolyte, evidencing strong interaction between Zn<sup>2+</sup> and N atoms in the additive.<sup>[43]</sup> With an increase in the mole ratio of ZnSO<sub>4</sub> and glycine, this spectral band shifts to a higher wavenumber, given that more Zn<sup>2+</sup> ions are available to interact with the additive with an increase in the Zn<sup>2+</sup>/glycine ratio. The Zn<sup>2+</sup> ions also interact with the additive through the COO<sup>-</sup> functional group as is evidenced in the Raman spectra with a wavenumber window ranging from 865–940 cm<sup>-1</sup>, Figure 3b. The COO<sup>-</sup> stretching vibration band exhibits a significant, positive shift from 889 cm<sup>-1</sup> in pure glycine solution to 916 cm<sup>-1</sup> as Zn<sup>2+</sup> numbers increase in the electrolyte.<sup>[44]</sup> The coordination between Zn<sup>2+</sup> and COO<sup>-</sup> was confirmed via FT-IR measurement, in which an upward shift was observed for the characteristic band for COO<sup>-</sup>, Figure 3c.<sup>[41]</sup>

<sup>1</sup>H nuclear magnetic resonance (NMR) on different solutions confirmed that the H originated from the –CH<sub>2</sub>– of the glycine with a characteristic peak located at ≈3.4 ppm, that shifts to ≈3.27 and ≈3.12 ppm for, respectively, 1 M ZnSO<sub>4</sub>–3 M glycine and 1 M ZnSO<sub>4</sub>–1 M glycine (Figure S6, Supporting Information). The negative shift evidence decreased electron density because of an inductive effect caused by the interaction between Zn<sup>2+</sup> and carboxy/amino group. To establish that the C–N and COO<sup>-</sup> vibration changes were primarily originating from the glycine–Zn<sup>2+</sup> interaction, rather than the glycine–H<sub>2</sub>O interaction, FT-IR was performed on glycine solution without the addition of ZnSO<sub>4</sub> salt. The O–H vibration band exhibited no significant change even in the 3 M glycine solution, confirming that the interaction between glycine and H<sub>2</sub>O is negligible (Figure S7, Supporting Information).

Using DFT, we determined possible Zn-ion solvation structures in aqueous electrolyte, starting with ZnSO<sub>4</sub> to Zn<sup>2+</sup> interacting with H<sub>2</sub>O and zwitterion glycine, (NH<sub>3</sub>)<sup>+</sup>CH<sub>2</sub>COO<sup>-</sup>. Glycine molecules exist in a zwitterion form in aqueous systems.<sup>[45]</sup> Adding glycine to the ZnSO<sub>4</sub> electrolyte impacts the hydration number in ZnSO<sub>4</sub> and Zn<sup>2+</sup>, making the transition from ZnSO<sub>4</sub> to Zn<sup>2+</sup> follow an alternative path. Glycine interaction with ZnSO<sub>4</sub> is concluded to be significantly strong, and spontaneous, as is seen in from energies in the forms of ZnSO<sub>4</sub>(H<sub>2</sub>O)<sub>3</sub>(NH<sub>3</sub>)<sup>+</sup>CH<sub>2</sub>COO<sup>-</sup> and ZnSO<sub>4</sub>(H<sub>2</sub>O)<sub>3</sub>.

Despite a lower energy state caused by glycine interaction with ZnSO<sub>4</sub>, the decoupling state for Zn<sup>2+</sup> and SO<sub>4</sub><sup>2-</sup> is achieved at a lower energy in the form of [Zn(H<sub>2</sub>O)<sub>3</sub>{(NH<sub>3</sub>)<sup>+</sup>CH<sub>2</sub>COO<sup>-</sup>}<sub>3</sub>]<sup>2+</sup> compared with that for [Zn(H<sub>2</sub>O)<sub>6</sub>]<sup>2+</sup>. This evidences that displacement of H<sub>2</sub>O from the inner solvation shell of Zn<sup>2+</sup> with (NH<sub>3</sub>)<sup>+</sup>CH<sub>2</sub>COO<sup>-</sup> is energetically favorable, and that the solvated H<sub>2</sub>O number is reduced from six in [Zn(H<sub>2</sub>O)<sub>6</sub>]<sup>2+</sup> to three in [Zn(H<sub>2</sub>O)<sub>3</sub>{(NH<sub>3</sub>)<sup>+</sup>CH<sub>2</sub>COO<sup>-</sup>}<sub>3</sub>]<sup>2+</sup>, Figures 3d,e. The impact of glycine on H<sub>2</sub> evolution from the view of deprotonation energy is presented in Figure 3f–h. Glycine alters deprotonation, and deprotonation of H<sub>2</sub>O in [Zn(H<sub>2</sub>O)<sub>6</sub>]<sup>2+</sup> remains more energetically favorable than that in glycine-bonded states, Figure 1i. The solvated H<sub>2</sub>O impact is minimized with the reduced number of solvated H<sub>2</sub>O molecules in the as-designed solvation structure, to suppress H<sub>2</sub> evolution and parasitic reactions, Figure 3i.

Findings from flame tests conducted on glass fiber soaked with electrolyte demonstrated that the addition of glycine did not compromise the nonflammability of the aqueous electrolyte (Figure S8, Supporting Information). The impact of glycine on the wettability of the electrolyte was assessed via sessile-drop contact-angle measurement (Figure S9, Supporting Information). The electrolyte with additive exhibited a decreased contact angle, compared with that of bare ZnSO<sub>4</sub> electrolyte. An improvement in the wettability of electrolyte benefits Zn plating/stripping because it influences the energy barrier for Zn nucleation and evolution.

The stability of the electrolyte on the Zn electrode was assessed using electrochemical impedance spectroscopy (EIS) on symmetric Zn|Zn cells (Figure S10, Supporting Information). Both bare ZnSO<sub>4</sub> electrolyte and electrolyte with additive exhibited similar charge transfer resistance in the fresh cell, however, the Zn|Zn symmetric cell impedance increased highly significantly following 7 days caused by an insulating

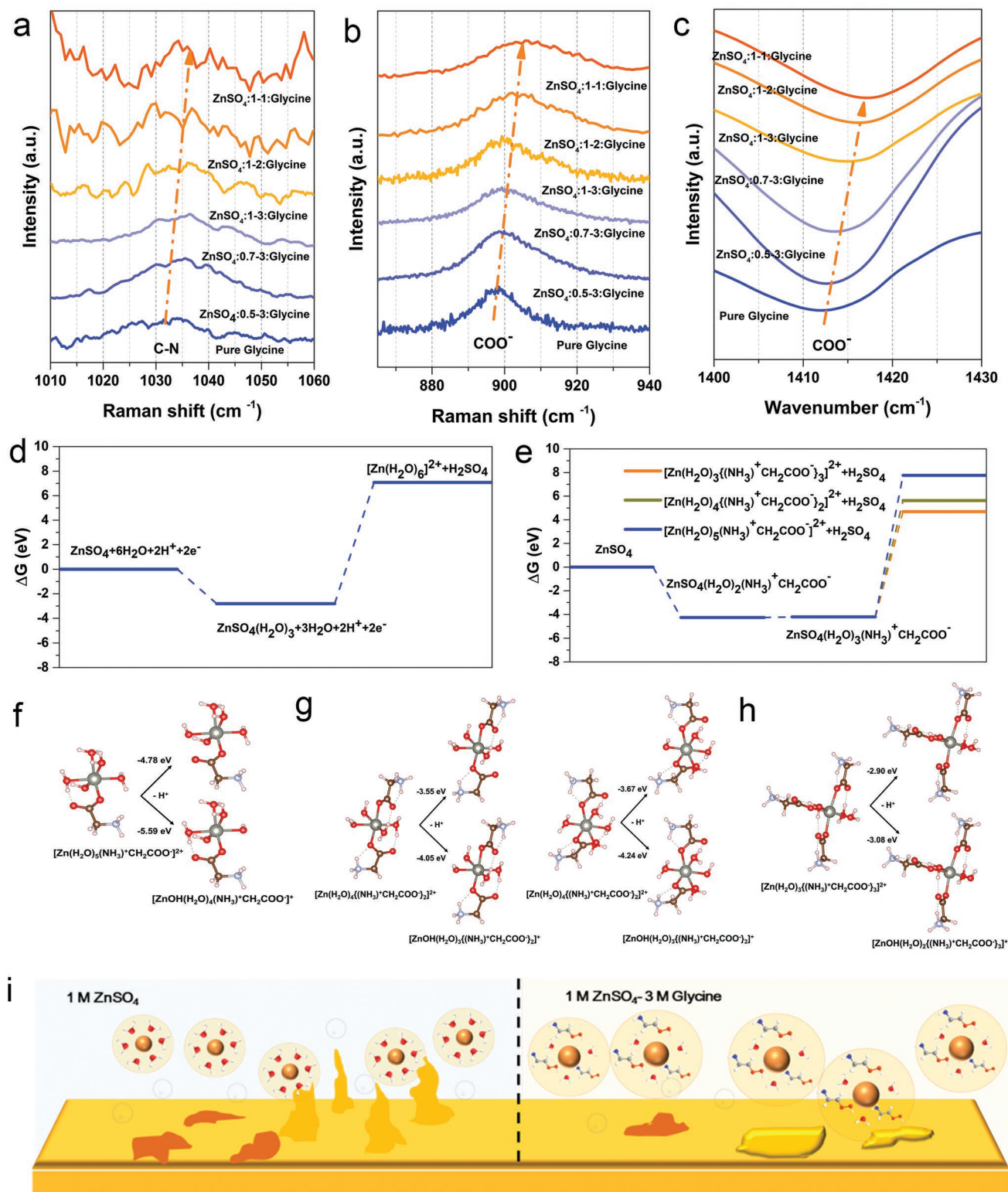


**Figure 3.** Characterization of zinc-ion solvation structure with glycine additive. a,b) Raman spectra for C–N (a) and COO<sup>-</sup> (b) stretching vibrations in ZnSO<sub>4</sub> electrolyte with glycine additive. c) FT-IR spectra for O–H stretching vibration in electrolyte with glycine. d,e) Reaction pathways for ZnSO<sub>4</sub> transition to Zn<sup>2+</sup> complex in aqueous electrolyte without (d) and with (e) glycine additive, as computed using DFT at 0 K. f–h) Deprotonation energy computed via DFT for [Zn(H<sub>2</sub>O)<sub>5</sub>(NH<sub>3</sub><sup>+</sup>CH<sub>2</sub>COO<sup>-</sup>)<sub>2</sub>]<sup>2+</sup> (f); [Zn(H<sub>2</sub>O)<sub>4</sub>{(NH<sub>3</sub><sup>+</sup>CH<sub>2</sub>COO<sup>-</sup>)<sub>2</sub>}]<sup>2+</sup> (g); and [Zn(H<sub>2</sub>O)<sub>3</sub>{(NH<sub>3</sub><sup>+</sup>CH<sub>2</sub>COO<sup>-</sup>)<sub>3</sub>}]<sup>2+</sup> (h). i) Schematics for zinc-ion solvation structure and interfacial side reaction in 1 M ZnSO<sub>4</sub> and 1 M ZnSO<sub>4</sub>-3 M glycine electrolyte.

layer formed during resting. In comparison, the impedance for 1 M  $\text{ZnSO}_4$ -3 M glycine remained almost unchanged. EIS findings evidence suppressed side reaction in the 1 M  $\text{ZnSO}_4$ -3 M glycine.

Additional evidence for the stability of the 1 M  $\text{ZnSO}_4$ -3 M glycine is available from the linear polarization measurements in which the 1 M  $\text{ZnSO}_4$ -3 M glycine electrolyte featured increased corrosion potential and reduced corrosion current and less corrosion (Figure S11, Supporting Information). With the solvated water molecules excluded from the inner solvation shell,  $\text{H}_2$  evolution is suppressed with glycine addition.

From LSV findings, the current response for 1 M  $\text{ZnSO}_4$ -3 M glycine electrolyte is apparently insignificant compared with 1 M  $\text{ZnSO}_4$  electrolyte (Figure S12, Supporting Information). A reduced tendency toward  $\text{H}_2$  evolution was confirmed in digital images of the electrolysis bath (Figure S13, Supporting Information). During negative scanning, significant bubbles were generated on the stainless steel mesh, in comparison, insignificant bubbling was observed for the electrolyte with glycine additive. The ionic conductivities of the various electrolytes were tested and findings (Figure S14, Supporting Information) evidenced that the 1 M  $\text{ZnSO}_4$ -3 M glycine electrolyte is comparable to the bare 1 M  $\text{ZnSO}_4$  electrolyte.

#### 2.4. Cycle Stability of As-Designed Solvation Structure

The positive impact of reducing the solvated water in the as-designed solvation structure in improving the stability of Zn plating/stripping was determined via long-term galvanostatic cycling of Zn|Zn symmetric cells. Under identical current density of 1  $\text{mA cm}^{-2}$  and areal capacity of 1  $\text{mAh cm}^{-2}$ , the bare  $\text{ZnSO}_4$  electrolyte exhibited a rapid reduction in polarization voltage, and the symmetric Zn|Zn cells failed following  $\approx 350$  h, **Figure 4a**, because of a short-circuit from the accumulation of detached, “dead” zinc and insulating by-products from  $\text{H}_2$  evolution.

In contrast, electrolytes with glycine additive exhibited boosted stability in the Zn|Zn symmetric cells, with the 1 M  $\text{ZnSO}_4$ -3 M glycine electrolyte exhibiting stable cycling beyond 1500 h. Zn|Zn cells tested in electrolytes with differing quantities of glycine demonstrated that cycling life was extended with the concentration of glycine (Figure S15, Supporting Information), and confirmed the positive impact of reducing solvated water with glycine additive for Zn plating/stripping.

To evaluate the performance of the as-designed electrolyte, increased current density and areal current capacity were applied and under a current density of 5  $\text{mA cm}^{-2}$ , the 1 M  $\text{ZnSO}_4$ -3 M glycine electrolytes exhibited a long cycling life of 700 h, whereas bare  $\text{ZnSO}_4$  failed following  $\approx 150$  h of cycling, **Figure 4b**. The designed electrolyte with additive outperformed bare  $\text{ZnSO}_4$  electrolyte at a greater current areal capacity of 5  $\text{mAh g}^{-1}$ , in cycling stability in symmetric Zn|Zn cells, **Figure 4c**. In addition, rate performance for Zn|Zn cells was carried out under current density from 0.5 to 10  $\text{mA cm}^{-2}$ . An unstable polarization induced by short-circuiting took place in the bare  $\text{ZnSO}_4$  electrolyte during testing, whilst the 1 M  $\text{ZnSO}_4$ -3 M glycine electrolyte demonstrated a stable voltage profile, **Figure 4d**.

The boosted electrochemical performance for the Zn|Zn symmetric cells is a result of controlled changes in solvation structure in the 1 M  $\text{ZnSO}_4$ -3 M glycine electrolyte to reduce solvated  $\text{H}_2\text{O}$  molecules and suppress  $\text{H}_2$  evolution and parasitic reactions. Zn|Zn symmetric cells following 100 h cycling were dismantled and the extracted Zn electrodes were subjected to X-ray diffraction (XRD) measurement to determine corrosion during cycling, **Figure 4e**. In the bare  $\text{ZnSO}_4$  electrolyte, a significant peak is exhibited at  $\approx 9.8^\circ$  which is indexed to  $\text{Zn}_4\text{SO}_4(\text{OH})_6 \cdot x\text{H}_2\text{O}$  by-product. The detection of the  $\text{Zn}_4\text{SO}_4(\text{OH})_6 \cdot x\text{H}_2\text{O}$  by-product evidences highly significant side reactions triggered by  $\text{H}_2$  evolution in the  $\text{ZnSO}_4$  electrolyte.<sup>[46]</sup> Following the addition of 3 M glycine, the  $\text{Zn}_4\text{SO}_4(\text{OH})_6 \cdot x\text{H}_2\text{O}$  by-product peak became faint, confirming the corrosion on the Zn electrode is significantly suppressed.

$\text{H}_2$  released during reversible Zn plating/stripping was quantified via in situ electrochemical gas chromatography (EC-GC) measurement. Zn metal was employed as a working and counter electrode in a home-made two-electrode device, which was subjected to reversible Zn plating/stripping at a current density 5  $\text{mA cm}^{-2}$  and an areal current capacity 2.5  $\text{mAh cm}^{-2}$  (**Figure S16**, Supporting Information). As was shown in the GC spectra (**Figure S17**, Supporting Information),  $\text{O}_2$  and  $\text{N}_2$ , that originate from the air were detected also with intensity remaining unchanged. In contrast, the  $\text{H}_2$  characteristic peak at  $\approx 5.55$  min exhibits an upward trend in intensity in Zn plating/stripping, **Figures 4f,g**. Further analyses demonstrated that the  $\text{H}_2$  in the bare  $\text{ZnSO}_4$  electrolyte increased from 0.914  $\mu\text{mol L}^{-1}$  in the first 15 min to 2.49  $\mu\text{mol L}^{-1}$  in 225 min. Compared with  $\text{ZnSO}_4$ ,  $\text{H}_2$  in 1 M  $\text{ZnSO}_4$ -3 M glycine electrolyte is just 0.168  $\mu\text{mol L}^{-1}$  in 15 min and gradually increased to 0.802  $\mu\text{mol L}^{-1}$  in 225 min, **Figure 4h**. Swelling occurred in both electrolytes, which evidences the suppression of  $\text{H}_2$  evolution in 1 M  $\text{ZnSO}_4$ -3 M glycine. Digital images of Zn|Zn symmetric cells following cycling showed that the battery in 1 M  $\text{ZnSO}_4$  broke open because of  $\text{H}_2$  accumulation, whilst the battery in 1 M  $\text{ZnSO}_4$ -3 M glycine electrolyte remained intact (**Figure S18**, Supporting Information).

To determine the impact on Zn reversibility of the designed solvation structure, digital and scanning electron microscopy (SEM) images were taken of the cycled Zn electrode. These showed that the surface on the Zn electrode in bare  $\text{ZnSO}_4$  electrolyte becomes “rougher” with cycling. In contrast, the Zn electrode from cycling in 1 M  $\text{ZnSO}_4$ -3 M glycine was “smooth” (**Figure S19**, Supporting Information). Concurrently, from the SEM images, the loose and inhomogeneous layer was observed on the Zn surface cycling in bare  $\text{ZnSO}_4$  electrolyte, which was composed of insulating dead zinc and corrosion by-product, whilst Zn deposition was compact and homogeneous in the 1 M  $\text{ZnSO}_4$ -3 M glycine electrolyte (**Figure S20**, Supporting Information).

To determine the versatility of the designed solvation structure, the glycine additive was applied also to the  $\text{ZnCl}_2$ -based electrolyte. Zn|Zn symmetric cells stability increased from 311 h in bare  $\text{ZnCl}_2$  electrolyte to  $>2000$  h, as glycine concentration was increased gradually to 3 M. Importantly, the electrolytes with additive outperformed the bare  $\text{ZnCl}_2$  in greater current density and areal current capacity (**Figure S21**, Supporting Information). The cycled Zn electrode in the 1 M  $\text{ZnCl}_2$ -3 M

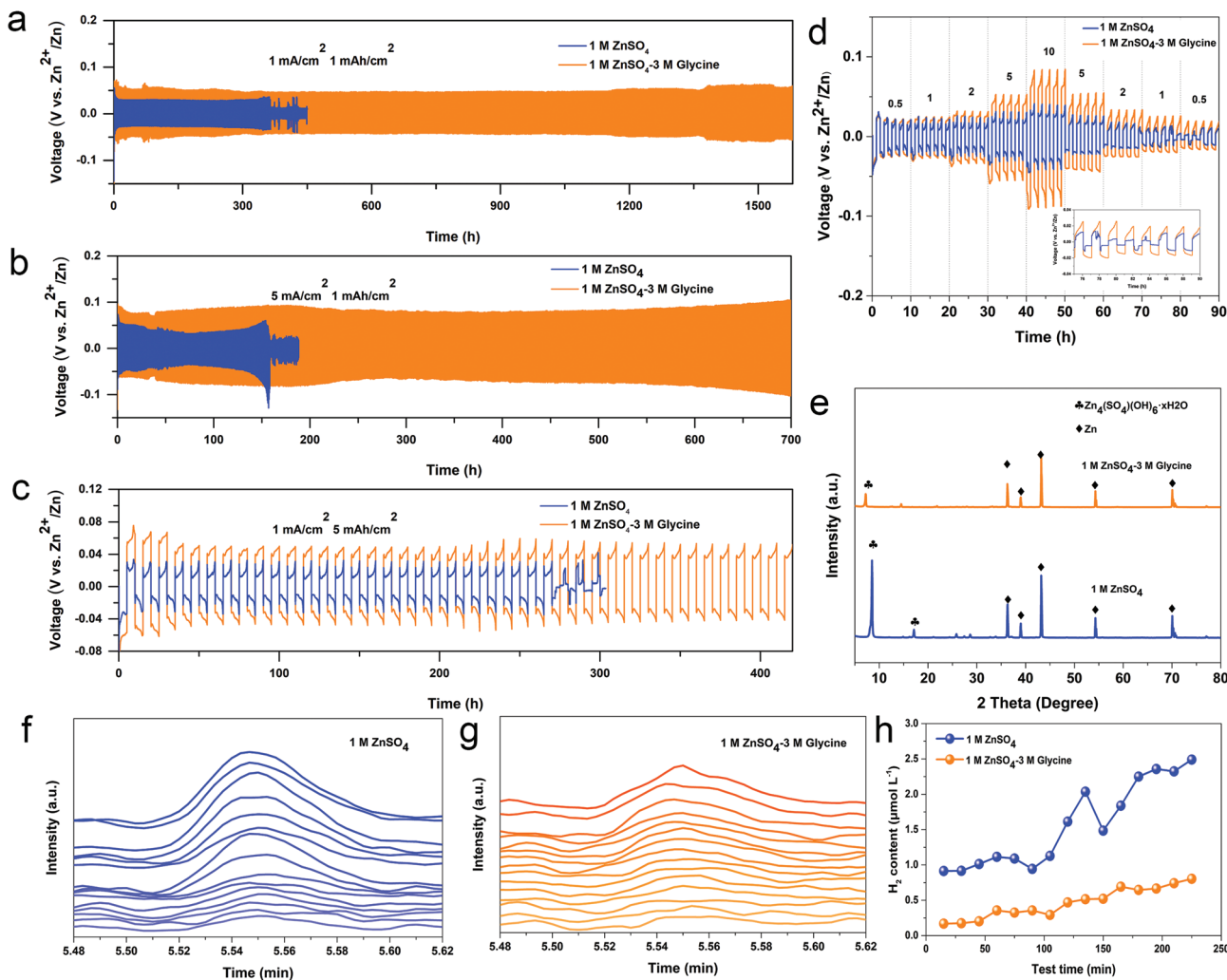


**Figure 4.** Plating/stripping cycling stability for Zn|Zn symmetric cells. a–c) Long-term galvanostatic cycling performance in 1 M ZnSO<sub>4</sub> and designed 1 M ZnSO<sub>4</sub>-3 M glycine electrolyte at 1 mA cm<sup>-2</sup> and areal capacity 1 mA h cm<sup>-2</sup> (a); 5 mA cm<sup>-2</sup> and areal capacity 1 mA h cm<sup>-2</sup> (b); and 1 mA cm<sup>-2</sup> and areal capacity 5 mA h cm<sup>-2</sup> (c). d) Rate performance for Zn|Zn symmetric cells. e) XRD spectra for Zn electrodes in electrolyte following 100 h cycling. f–h) In situ EC–GC profile confirming H<sub>2</sub> evolution. f, g) EC–GC profiles during Zn plating/stripping (5 mA cm<sup>-2</sup>) in 1 M ZnSO<sub>4</sub> (f) and 1 M ZnSO<sub>4</sub>-3 M glycine (g) electrolyte, and h) plot of H<sub>2</sub> during the in situ EC–GC measurement.

glycine exhibited homogeneous Zn deposition (Figures S22 and 23, Supporting Information) similar to ZnSO<sub>4</sub>-based electrolytes. XRD spectra for the Zn electrode in the 1 M ZnCl<sub>2</sub>-3 M glycine electrolyte exhibited no apparent Zn<sub>5</sub>(OH)<sub>8</sub>Cl<sub>2</sub>·H<sub>2</sub>O by-product following even 300 h cycling (Figure S24, Supporting Information), confirming that H<sub>2</sub> evolution induced corrosion was significantly suppressed in the ZnCl<sub>2</sub> electrolyte.

## 2.5. Zn Deposition and Reversibility of Designed Electrolyte

The inhibition of Zn dendrite formation in the 1 M ZnSO<sub>4</sub>-3 M glycine electrolyte was determined in transparent homemade Zn|Cu asymmetric cells. To monitor dendrite growth, optical microscopy was used to capture images of the Cu electrode during Zn plating/stripping. As is shown in Figure 5a, uneven Zn deposition was observed on the initial, smooth and flat Cu

edge during Zn plating, which then developed into zinc dendrites. This evidences significant Zn dendrite formation in 1 M ZnSO<sub>4</sub> electrolyte. In comparison, a Zn layer deposited on the Cu electrode in 1 M ZnSO<sub>4</sub>-3 M glycine electrolyte was smooth and had no apparent Zn dendrite, Figure 5b. This homogeneous Zn deposition is attributed to the greater nucleation overpotential resulting from the stronger coordination between Zn<sup>2+</sup> and glycine molecules in the solvation structure, defined by:

$$r = 2 \frac{\gamma V_m}{F|\eta|} \quad (3)$$

where  $r$  is critical Zn nucleus radius,  $\gamma$  the surface energy of the Zn-electrolyte interface,  $V_m$  the molar volume of Zn,  $F$  the Faraday constant, and  $\eta$  the nucleation overpotential. The relationship between the Zn nucleus radius and nucleation overpotential shown in Equation (3) underscores that high



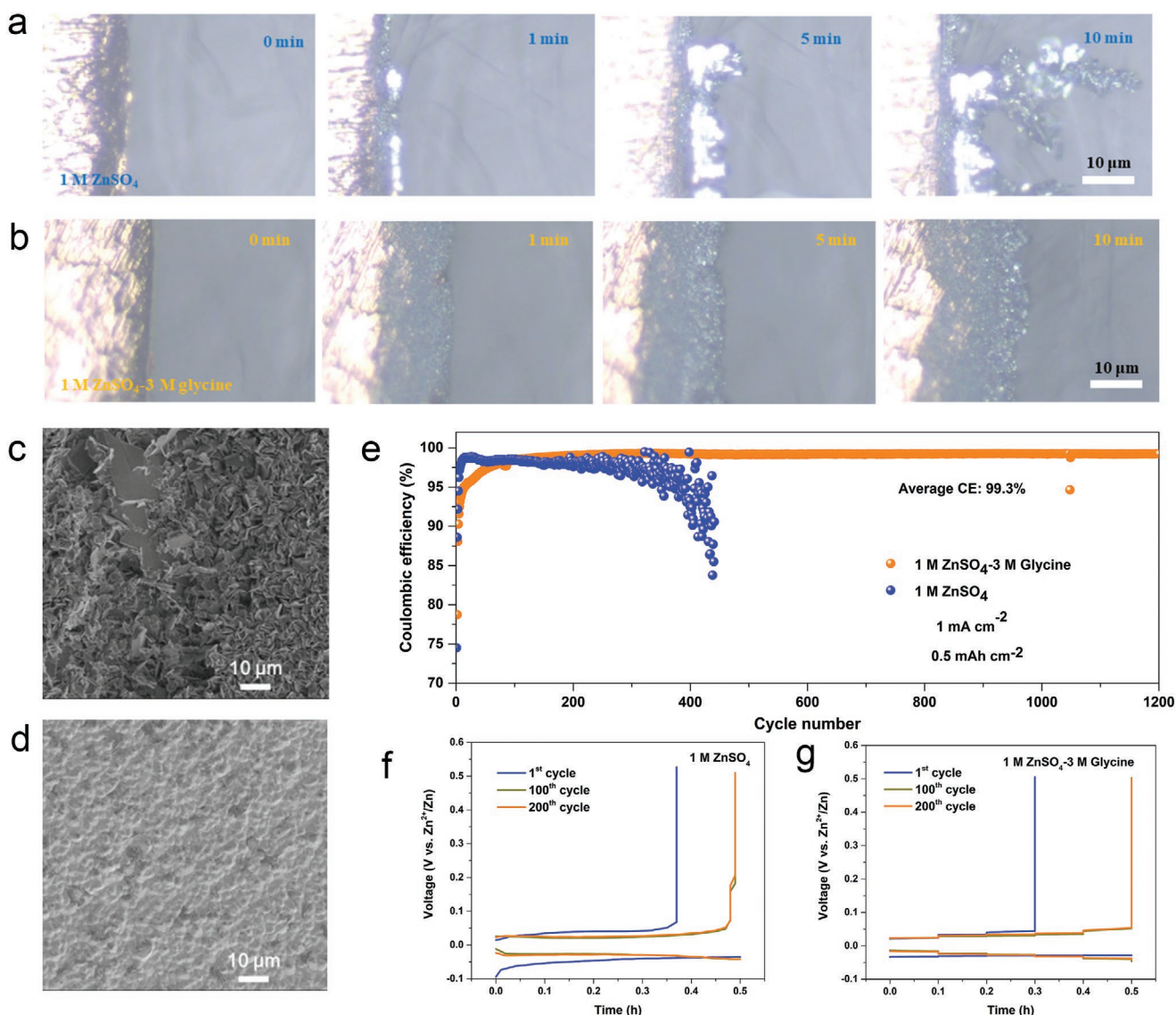


**Figure 5.** Zn deposition behaviour and reversibility. a,b) In situ optical microscopy images of cross-sectional Zn deposition morphology on Cu-foil in 1 M ZnSO<sub>4</sub> (a) and 1 M ZnSO<sub>4</sub>-3 M glycine (b) electrolyte in Zn|Cu asymmetrical cells. c,d) SEM images of Zn deposition on Cu electrode in Zn|Cu asymmetric cells at 1 mA cm<sup>-2</sup> and 0.5 mAh cm<sup>-2</sup> following 50 cycles in 1 M ZnSO<sub>4</sub> (c) and 1 M ZnSO<sub>4</sub>-3 M glycine (d) electrolyte. e) Coulombic efficiency (CE) for Zn plating/stripping on Cu. f,g) Corresponding voltage profile for Cu/Zn cells in 1 M ZnSO<sub>4</sub> electrolyte (f) and 1 M ZnSO<sub>4</sub>-3 M glycine electrolyte (g) at differing cycles.

nucleation overpotential leads to a fine-grained and homogeneous Zn deposition.<sup>[47–49]</sup>

Zn|Cu asymmetric cells were subject to repeated Zn plating/stripping under current density of 1 mA cm<sup>-2</sup> and areal current capacity 0.5 mAh cm<sup>-2</sup>, to determine the reversibility of different electrolytes. As is presented in Figure 5e, the bare ZnSO<sub>4</sub> electrolyte exhibited a stable CE of ≈97.3% for ≈200 cycles, then significantly decreased to 85% following ≈440 cycles. This comparatively low value for CE for bare ZnSO<sub>4</sub> electrolyte is attributed to the irreversible reaction induced by significant H<sub>2</sub> evolution and corrosion on the Zn electrode. For the 1 M Zn ZnSO<sub>4</sub>-3 M glycine electrolyte, the Zn|Cu cells reversibly plating/stripping for more than 1200 cycles and a high average CE of ≈99.3% was maintained. The boosted reversibility of the

1 M ZnSO<sub>4</sub>-3 M glycine electrolyte is attributed to the reduced solvated water, which has a greater tendency against H<sub>2</sub> evolution than the free water. Figures 5f,g compare voltage profiles for Zn|Cu cells in 1 M ZnSO<sub>4</sub> and 1 M ZnSO<sub>4</sub>-3 M glycine electrolyte. The cell in 1 M ZnSO<sub>4</sub>-3 M glycine electrolyte exhibited a higher voltage polarization than the cell in bare ZnSO<sub>4</sub> electrolyte. The higher voltage polarization resulted from the strong coordination between Zn<sup>2+</sup> and glycine molecules which leads to greater desolvation energy.

The morphology of the Zn deposited on Cu-foil was assessed. Digital images of the Cu electrode following 50 cycles of deposition showed that the Zn layer deposited in the 1 M ZnSO<sub>4</sub>-3 M glycine electrolyte was homogeneous when compared with that in the bare ZnSO<sub>4</sub> electrolyte (Figure S26, Supporting

Information). SEM images evidenced that the Zn layer in bare ZnSO<sub>4</sub> electrolyte featured “loose” structures indexed to thick “dead” Zn, and insulated corrosion by-product, Figure 5c. In comparison, Zn deposition in 1 M ZnSO<sub>4</sub>–3 M glycine electrolyte was “ultra-flat and compact” without dendrites, Figure 5d. The glycine additive also improved Zn|Cu CE in ZnCl<sub>2</sub>-based electrolyte (Figure S27, Supporting Information) and resulted in dendrite-free Zn deposition (Figures S28 and 29, Supporting Information). The high value for CE for Zn|Cu, together with the dendrite-free Zn deposition, confirms that H<sub>2</sub> evolution and corrosion are minimized in the electrolyte with the additive.

## 2.6. Full Cell Performance of Electrolyte

To evaluate the practical application of the as-designed electrolyte in full cells, a cathode material, PANI (highly conductive polyaniline), was synthesized (Figure S30, Supporting Information)

and paired with the Zn-metal anode to prepare Zn|PANI full cells. Figure 6a presents the cycling performance for the Zn|PANI full cell under current density of 0.2 A g<sup>-1</sup>. Both the bare ZnSO<sub>4</sub> and 1 M ZnSO<sub>4</sub>–3 M glycine electrolytes exhibited a similar reversible capacity of ≈200 mAh g<sup>-1</sup> in the initial 5 cycles. However, the Zn|PANI full cell with 1 M ZnSO<sub>4</sub> electrolyte exhibited a rapid capacity decay in the following 50 cycles, and a specific capacity of ≈110 mAh g<sup>-1</sup> only was maintained following 300 cycles. This cycling stability is significantly inferior to that for 1 M ZnSO<sub>4</sub>–3 M glycine electrolyte, in which a high reversible capacity of ≈200 mAh g<sup>-1</sup> was exhibited. The rate performance for Zn|PANI full cell in different electrolytes was determined under differing current densities. The Zn|PANI full cell exhibited reversible capacity of 200, 150, 105, and 70 mAh g<sup>-1</sup> as current density increased from 0.2 to 2 A g<sup>-1</sup>, which is significantly greater than that for bare ZnSO<sub>4</sub> electrolyte, Figure 6b. Importantly, capacity was restored to initial levels when the current density was

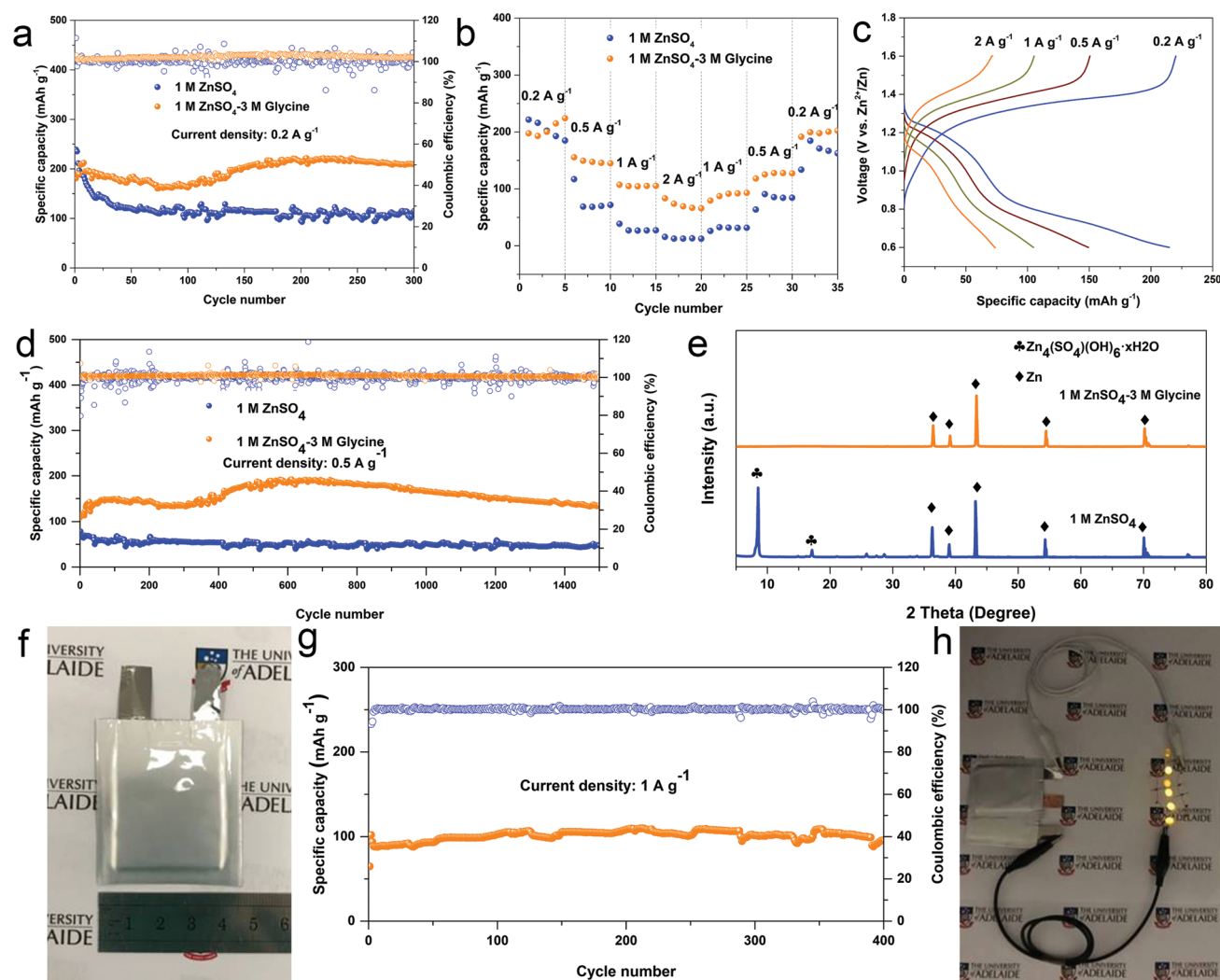


**Figure 6.** Zn|PANI full cell electrochemical performance. a) Cycling performance at current density 0.2 A g<sup>-1</sup>. b) Rate performance at current density ranging from 0.2 to 2 A g<sup>-1</sup>, and c) corresponding charge–discharge profile at different current density. d) Long-term cycling performance at 0.5 A g<sup>-1</sup>. e) XRD spectra for Zn anode stripped from Zn|PANI full cells following 50 cycles. f) Digital image of Zn|PANI pouch cell. g) Cycling performance for Zn|PANI pouch cell at 1 A g<sup>-1</sup>. h) Two pouch cells power six yellow LEDs.

decreased gradually, evidencing excellent reversibility of the full cells.

Charge–discharge curves from rate testing evidence the low polarization of the Zn|PANI full cells in the electrolyte with glycine additive, Figure 6c. The full cells were subjected to high current density of  $0.5 \text{ A g}^{-1}$  to determine long-term cycling stability. As is confirmed in Figure 6d, the  $1 \text{ M ZnSO}_4\text{-}3 \text{ M}$  glycine electrolyte outperformed the bare  $\text{ZnSO}_4$  electrolyte, with capacity of  $132 \text{ mAh g}^{-1}$  exhibited following 1500 cycles. To confirm the function of glycine in the full cells, the Zn-metal anode was stripped from the Zn|PANI full cells following 50 cycles. As is apparent from Figure 6e (and Figure S31, Supporting Information), similar to the results in Zn|Zn and Zn|Cu cells, the Zn electrode of the Zn|PANI full cells does not show the presence of  $\text{Zn}_4\text{SO}_4(\text{OH})_6 \cdot x\text{H}_2\text{O}$  by-product and is also dendrite-free of Zn deposition (Figure S31, Supporting Information).

The electrochemical performance of the electrolyte was assessed in a soft-packed cell. In a Zn|PANI pouch cell of 4.5 cm width and 6.0 cm length, Figure 6f, a high capacity of  $\approx 100 \text{ mAh g}^{-1}$  was exhibited under a high current density of  $1 \text{ A g}^{-1}$  following 400 cycles, Figure 6h. The pouch cell powered six yellow light-emitting diodes, confirming the efficacy of the pouch cell. As shown in Tables S1 and S2 (Supporting Information), our Zn|PANI performance is comparable to the previous reports. Additionally, the designed electrolyte was confirmed for the other cathode materials. As shown in Figure S32 (Supporting Information), the cycling and rate performance of the Zn|LiFePO<sub>4</sub> full cell is boosted when glycine is added to the electrolyte.

### 3. Conclusions

We have demonstrated for the first time, using a combined gas chromatography experiment and computation, that H<sub>2</sub> evolution primarily originates from solvated water, rather than free water without interaction with Zn<sup>2+</sup>. H<sub>2</sub> evolution occurs at a more negative potential than zinc reduction because of the high overpotential against H<sub>2</sub> evolution on Zn metal. Glycine, an environmentally friendly and low-cost additive, can be used to minimize the impact of solvated water on Zn-metal anodes and to control the Zn<sup>2+</sup>-solvation structure. Combined, judicious experiment (including, Raman spectroscopy and Fourier-transform infrared (FT-IR) spectroscopy), and theoretical computation (DFT) evidences that solvation structure with reduced solvated water molecules results in 3 M glycine in 1 M ZnSO<sub>4</sub> electrolyte because of the strong coordination ability of glycine to Zn<sup>2+</sup>. The glycine-electrolyte suppresses H<sub>2</sub> evolution, reduces corrosion, and promotes uniform Zn deposition in Zn|Zn and Zn|Cu cells when compared with bare ZnSO<sub>4</sub> electrolyte.

Zn|PANI (polyaniline) full cells exhibited boosted electrochemical performance in 1 M ZnSO<sub>4</sub>-3 M glycine electrolytes. A high reversible capacity of  $100 \text{ mAh g}^{-1}$  was obtained in a practical Zn|PANI pouch cell.

We conclude that this new understanding of electrochemistry of H<sub>2</sub> evolution can be used for Zn-metal anode protection and improved the design of relatively low-cost and safe AZIBs for practical large-scale energy storage.

Findings will be of immediate benefit in electrolyte design for high-performance rechargeable AZIBs and therefore of wide interest to researchers and manufacturers.

### Supporting Information

Supporting Information is available from the Wiley Online Library or from the author.

### Acknowledgements

Financial support provided by the Australian Research Council (ARC) (FL210100050, LP160101629, DP210101486, DP200101862, and LE180100141) is gratefully acknowledged. J.A.Y acknowledges assistance of resources and services from the National Computational Infrastructure (NCI) that was supported by Australian Government through ANUMAS scheme in joint project with N.B. J.L. was supported by grants from the National Natural Science Foundation of China (No. 52102276).

Open access publishing facilitated by The University of Adelaide, as part of the Wiley - The University of Adelaide agreement via the Council of Australian University Librarians.

### Conflict of Interest

The authors declare no conflict of interest.

### Data Availability Statement

The data that support the findings of this study are available on request from the corresponding author. The data are not publicly available due to privacy or ethical restrictions.

### Keywords

aqueous zinc-ion batteries, zinc-metal anodes, H<sub>2</sub> evolution, solvated water, zinc reduction

Received: July 25, 2022  
Revised: September 2, 2022  
Published online: October 17, 2022

- [1] D. Chao, S.-Z. Qiao, *Joule* **2020**, 4, 1846.
- [2] J. Hao, L. Yuan, B. Johannessen, Y. Zhu, Y. Jiao, C. Ye, F. Xie, S. Qiao, *Angew. Chem.* **2021**, 133, 25318.
- [3] Y. Zhang, F. Wan, S. Huang, S. Wang, Z. Niu, J. Chen, *Nat. Commun.* **2020**, 11, 2199.
- [4] X. Ji, *Energy Environ. Sci.* **2019**, 12, 3203.
- [5] H. Pan, Y. Shao, P. Yan, Y. Cheng, K. S. Han, Z. Nie, C. Wang, J. Yang, X. Li, P. Bhattacharya, K. T. Mueller, J. Liu, *Nat. Energy* **2016**, 1, 16039.
- [6] P. Ruan, S. Liang, B. Lu, H. J. Fan, J. Zhou, *Angew. Chem., Int. Ed.* **2022**, 61, e202200598.
- [7] S. Zuo, X. Xu, S. Ji, Z. Wang, Z. Liu, J. Liu, *Chem. - Eur. J.* **2021**, 27, 830.
- [8] J. Zheng, Q. Zhao, T. Tang, J. Yin, C. D. Quilty, G. D. Renderos, X. Liu, Y. Deng, L. Wang, D. C. Bock, C. Jaye, D. Zhang,

- E. S. Takeuchi, K. J. Takeuchi, A. C. Marschilok, L. A. Archer, *Science* **2019**, 366, 645.
- [9] M. Yu, N. Chandrasekhar, R. K. M. Raghupathy, K. H. Ly, H. Zhang, E. Dmitrieva, C. Liang, X. Lu, T. D. Kühne, H. Mirhosseini, I. M. Weidinger, X. Feng, *J. Am. Chem. Soc.* **2020**, 142, 19570.
- [10] J. Hao, X. Li, X. Zeng, D. Li, J. Mao, Z. Guo, *Energy Environ. Sci.* **2020**, 13, 3917.
- [11] W. He, S. Zuo, X. Xu, L. Zeng, L. Liu, W. Zhao, J. Liu, *Mater. Chem. Front.* **2021**, 5, 2201.
- [12] S. Zuo, J. Liu, W. He, S. Osman, Z. Liu, X. Xu, J. Shen, W. Jiang, J. Liu, Z. Zeng, M. Zhu, *J. Phys. Chem. Lett.* **2021**, 12, 7076.
- [13] Y. Wang, Z. Wang, F. Yang, S. Liu, S. Zhang, J. Mao, Z. Guo, *Small* **2022**, 2107033, 2107033.
- [14] L. Ma, S. Chen, N. Li, Z. Liu, Z. Tang, J. A. Zapien, S. Chen, J. Fan, C. Zhi, *Adv. Mater.* **2020**, 32, 1908121.
- [15] S. D. Pu, C. Gong, Y. T. Tang, Z. Ning, J. Liu, S. Zhang, Y. Yuan, D. Melvin, S. Yang, L. Pi, J. Marie, B. Hu, M. Jenkins, Z. Li, B. Liu, S. C. E. Tsang, T. J. Marrow, R. C. Reed, X. Gao, P. G. Bruce, A. W. Robertson, *Adv. Mater.* **2022**, 34, 2202552.
- [16] L. Yuan, J. Hao, C.-C. Kao, C. Wu, H.-K. Liu, S.-X. Dou, S.-Z. Qiao, *Energy Environ. Sci.* **2021**, 14, 5669.
- [17] L. Cao, D. Li, T. Pollard, T. Deng, B. Zhang, C. Yang, L. Chen, J. Vatamanu, E. Hu, M. J. Hourwitz, L. Ma, M. Ding, Q. Li, S. Hou, K. Gaskell, J. T. Fourkas, X. Yang, K. Xu, O. Borodin, C. Wang, *Nat. Nanotechnol.* **2021**, 16, 902.
- [18] Y.-P. Deng, R. Liang, G. Jiang, Y. Jiang, A. Yu, Z. Chen, *ACS Energy Lett.* **2020**, 5, 1665.
- [19] X. Xie, S. Liang, J. Gao, S. Guo, J. Guo, C. Wang, G. Xu, X. Wu, G. Chen, J. Zhou, *Energy Environ. Sci.* **2020**, 13, 503.
- [20] Z. Wang, J. Huang, Z. Guo, X. Dong, Y. Liu, Y. Wang, Y. Xia, *Joule* **2019**, 3, 1289.
- [21] M. Li, Z. Li, X. Wang, J. Meng, X. Liu, B. Wu, C. Han, L. Mai, *Energy Environ. Sci.* **2021**, 14, 3796.
- [22] L. Cao, D. Li, E. Hu, J. Xu, T. Deng, L. Ma, Y. Wang, X. Yang, C. Wang, *J. Am. Chem. Soc.* **2020**, 142, 21404.
- [23] Q. Zhang, Y. Ma, Y. Lu, X. Zhou, L. Lin, L. Li, Z. Yan, Q. Zhao, K. Zhang, J. Chen, *Angew. Chem., Int. Ed.* **2021**, 60, 23557.
- [24] N. Chang, T. Li, R. Li, S. Wang, Y. Yin, H. Zhang, X. Li, *Energy Environ. Sci.* **2020**, 13, 3527.
- [25] J. Hao, L. Yuan, C. Ye, D. Chao, K. Davey, Z. Guo, S. Qiao, *Angew. Chem., Int. Ed.* **2021**, 60, 7366.
- [26] C. Xu, B. Li, H. Du, F. Kang, *Angew. Chem., Int. Ed.* **2012**, 51, 933.
- [27] W. Cheng, H. Zhang, D. Luan, X. Wen, D. Lou, *Sci. Adv.* **2021**, 7, eabg2580.
- [28] Z. Tie, L. Liu, S. Deng, D. Zhao, Z. Niu, *Angew. Chem., Int. Ed.* **2020**, 59, 4920.
- [29] S. Chen, R. Lan, J. Humphreys, S. Tao, *Energy Storage Mater.* **2020**, 28, 205.
- [30] N. Li, G. Li, C. Li, H. Yang, G. Qin, X. Sun, F. Li, H.-M. Cheng, *ACS Appl. Mater. Interfaces* **2020**, 12, 13790.
- [31] J. Cao, D. Zhang, X. Zhang, Z. Zeng, J. Qin, Y. Huang, *Energy Environ. Sci.* **2022**, 15, 499.
- [32] L. Qian, W. Yao, R. Yao, Y. Sui, H. Zhu, F. Wang, J. Zhao, C. Zhi, C. Yang, *Adv. Funct. Mater.* **2021**, 31, 2105736.
- [33] P. Sun, L. Ma, W. Zhou, M. Qiu, Z. Wang, D. Chao, W. Mai, *Angew. Chem., Int. Ed.* **2021**, 60, 18247.
- [34] Y. Zhu, J. Yin, X. Zheng, A. H. Emwas, Y. Lei, O. F. Mohammed, Y. Cui, H. N. Alshareef, *Energy Environ. Sci.* **2021**, 14, 4463.
- [35] S. Chen, M. Zhang, P. Zou, B. Sun, S. Tao, *Energy Environ. Sci.* **2022**, 15, 1805.
- [36] Q. Zhang, Y. Ma, Y. Lu, L. Li, F. Wan, K. Zhang, J. Chen, *Nat. Commun.* **2020**, 11, 4463.
- [37] L. F. Scatena, M. G. Brown, G. L. Richmond, *Science* **2001**, 292, 908.
- [38] Y.-H. Wang, S. Zheng, W.-M. Yang, R.-Y. Zhou, Q.-F. He, P. Radjenovic, J.-C. Dong, S. Li, J. Zheng, Z.-L. Yang, G. Attard, F. Pan, Z.-Q. Tian, J.-F. Li, *Nature* **2021**, 600, 81.
- [39] K. Wippermann, J. Schultze, R. Kessel, J. Penninger, *Corros. Sci.* **1991**, 32, 205.
- [40] L. Suo, O. Borodin, T. Gao, M. Olguin, J. Ho, X. Fan, C. Luo, C. Wang, K. Xu, *Science* **2015**, 350, 938.
- [41] G. V. Novikova, A. I. Petrov, N. A. Staloverova, A. S. Samoilo, I. D. Dergachev, A. A. Shubin, *Spectrochim. Acta, A: Mol. Biomol. Spectrosc.* **2015**, 135, 491.
- [42] R. Fernandes de Farias, *Quim. Nova* **2002**, 25, 729.
- [43] C. Murli, S. M. Sharma, S. Karmakar, S. K. Sikka, *Phys. B: Condens. Matter* **2003**, 339, 23.
- [44] K. A. Khnykina, V. V. Kireev, N. V. Krunina, N. D. Kundikova, E. V. Verina, *2018 Global Smart Industry Conf., IEEE, Piscataway, NJ, USA* **2018**, <https://doi.org/10.1109/GloSIC.2018.8570138>.
- [45] M. Remko, B. M. Rode, *J. Phys. Chem. A* **2006**, 110, 1960.
- [46] T. Zhang, Y. Tang, G. Fang, C. Zhang, H. Zhang, X. Guo, X. Cao, J. Zhou, A. Pan, S. Liang, *Adv. Funct. Mater.* **2020**, 30, 2002711.
- [47] Z. Zhao, J. Zhao, Z. Hu, J. Li, J. Li, Y. Zhang, C. Wang, G. Cui, *Energy Environ. Sci.* **2019**, 12, 1938.
- [48] A. Pei, G. Zheng, F. Shi, Y. Li, Y. Cui, *Nano Lett.* **2017**, 17, 1132.
- [49] Y. Zhang, M. Zhu, K. Wu, F. Yu, G. Wang, G. Xu, M. Wu, H.-K. Liu, S.-X. Dou, C. Wu, *J. Mater. Chem. A* **2021**, 9, 4253.